

# Numerical model for predicting experimental effects in enantioselective Raman spectroscopy

Niklas Jüngst<sup>1,5</sup> · Andrew P. Williamson<sup>1</sup> · Johannes Kiefer<sup>1,2,3,4</sup> 

Received: 31 December 2016 / Accepted: 28 February 2017 / Published online: 3 April 2017  
© Springer-Verlag Berlin Heidelberg 2017

**Abstract** Chiroptical methods facilitating enantioselective quantitative measurements with good temporal and spatial resolution are highly desirable for process monitoring, e.g., during the production of pharmaceuticals. The recently proposed enantioselective Raman (esR) spectroscopy has a great potential in this respect. The a priori knowledge of how the settings of the experimental parameters will affect the measurement is crucial to avoid systematic errors and to build an optimized setup. This work presents a ray tracing-based model for the simulation of light scattering experiments and uses it to investigate the effects of experimental parameters in esR spectroscopy. The main advancement to the previous work is that the model is implemented in 3D and takes a large variety of effects into account. The laser beam is considered as a Gaussian beam. The light scattered from the different volume elements illuminated by the laser is traced through the

optical components of the signal collection system. The results indicate that the enantioselective characteristics of the method that were proposed for 1D are still valid in a 3D geometry. The contrast and sharpness in the polarization-resolved intensity distributions are moderately reduced compared to the idealized case. This is very promising for the practical application of the esR technique. The results confirm that it can be applied for a broad range of settings and substances.

## 1 Introduction

Biological systems usually exhibit a high degree of chirality. As an example, amino acids, which govern the human metabolism, appear in a certain enantiomeric configuration, so that the two enantiomers of a chiral substance are catabolized differently [1, 2]. Consequently, most of the drugs used in a clinical and therapeutic context are chiral to effectively interact with the receptors [3, 4]. When using chiral drugs, one enantiomer might exhibit the desired pharmacological effect, while the other one might show a weaker, nonexistent, antagonistic, or even toxic response [1]. Due to historical incidents, for example, the use of the sedative drug thalidomide [5], chiral drugs tend to be brought to market in an enantiopure form. While 30% of the drugs that appeared on the US market in 1990 were racemic mixtures, none of the new drugs in 2006 was racemic [6]. The understanding of the connection between biological reactions and chirality has become a governing issue in the research and development departments of the pharmaceutical industry within the last three decades [7].

Enantiopure substances are gaining importance not only in the pharmaceutical sector. Around 40% of the globally used pesticides exhibit chirality and react enantioselectively

---

**Electronic supplementary material** The online version of this article (doi:10.1007/s00340-017-6685-z) contains supplementary material, which is available to authorized users.

---

✉ Johannes Kiefer  
jkiefer@uni-bremen.de

- <sup>1</sup> Technische Thermodynamik, Universität Bremen, Badgasteiner Str. 1, 28359 Bremen, Germany
- <sup>2</sup> School of Engineering, University of Aberdeen, Aberdeen AB24 3UE, UK
- <sup>3</sup> Erlangen Graduate School in Advanced Optical Technologies (SAOT), Universität Erlangen-Nürnberg, Erlangen, Germany
- <sup>4</sup> MAPEX Center for Materials and Processes, University of Bremen, Bremen, Germany
- <sup>5</sup> Present Address: IVG, Institute for Combustion and Gas Dynamics, University of Duisburg-Essen, 47048 Duisburg, Germany

with the target plant. As an example, the D-(–)-enantiomer of the herbicide napropamide, which is commonly applied to fruits, vegetables, and crops, showed an eightfold higher activity to different grasses than its mirror image, the L-(+)-enantiomer [8]. Applying enantiopure pesticides, which contain exclusively the active enantiomer, reduces, on one hand, the production costs due to a lower dosage and protects the environment from potentially toxic pesticides on the other hand [8].

The demand for enantiopure substances calls for purification processes that accumulate the active enantiomer and reduce the fraction of the undesired isomer. This, in turn, establishes the need for suitable techniques for quality control and process monitoring by determining the enantiomeric ratio and the overall concentration of the chiral species with sufficient temporal resolution. However, enantiomeric discrimination is difficult, because the two enantiomers of a chiral substance exhibit the same physical and chemical properties [9].

In principle, NMR spectroscopy can measure the enantiomeric purity when chiral agents are added [10]. Other established procedures are vibrational circular dichroism (VCD) and Raman optical activity (ROA) [11–13]. Both exploit the vibrational optical activity of a chiral substance, which describes the influence on vibrational spectra when using circularly polarized light and yields besides to the enantiomeric configuration detailed structural information about the analyzed molecule [14]. Other spectroscopic approaches for enantiomeric discrimination include cavity ring-down polarimetry [15], surface enhanced Raman spectroscopy [16], and microwave spectroscopy [17].

As an alternative, enantioselective Raman (esR) spectroscopy was recently introduced [18] based on the considerations of how the optical activity in a chiral sample modifies the polarization state of the incident laser beam and the Raman signal [19]. The (+)- and the (–)-enantiomer rotate the polarization by the exactly same angle but in opposite direction. For enantioselective measurements, this inherent symmetry of the scattered light in terms of polarization rotation has to be broken. Otherwise, looking at the vertically and horizontally polarized signal components leads to identical Raman spectra for both enantiomers. Inserting an achromatic half-wave plate in the signal path breaks this symmetry and results in different resulting rotation angles for the two samples. This procedure leads to a redistribution of horizontally and vertically polarized intensities and enables the unambiguous assignment of a pair of horizontally and vertically polarized signal intensities to an enantiomer composition [20]. An important feature of the method is that the optical activity of the sample is utilized. This means that the effects can be observed for Raman signals

of both, the chiral substance and the solvent. Consequently, chiral molecules at low concentration may still lead to reasonable optical activity and hence allow a quantitative measurement, although their Raman peaks are hardly visible in the spectrum.

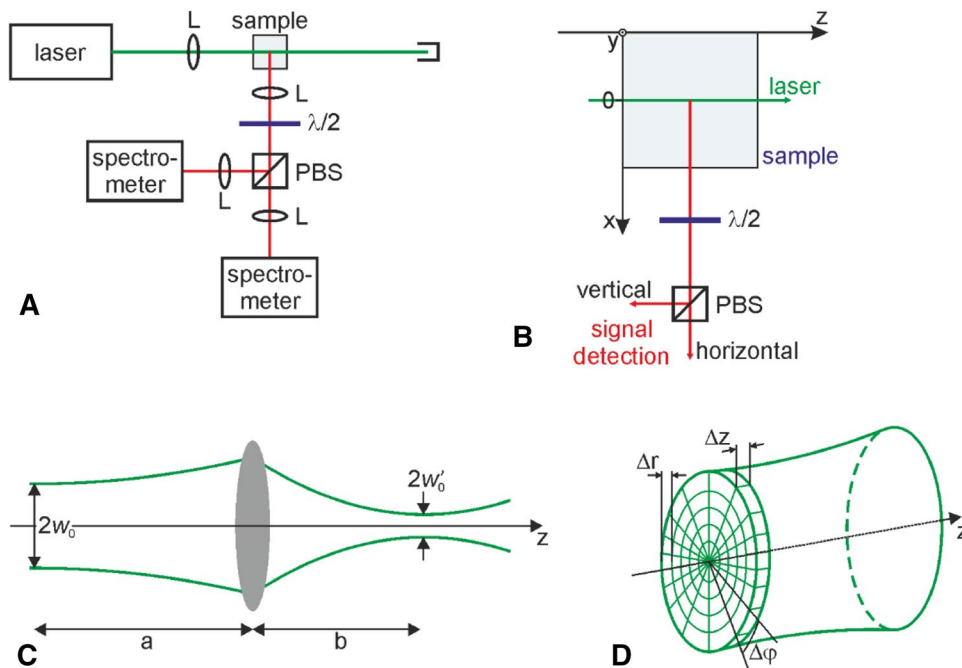
In the previous theoretical work on this method [18, 20], the laser beam was considered as a one-dimensional line and the solid angle of signal collection was considered to be  $\sim 0$ . Under these assumptions, a clear discrimination between the enantiomers and a quantitative measurement was possible. The present work makes a substantial step towards a real-world application. For this purpose, a detailed numerical model is presented that allows taking 3D-effects into account and that facilitates studying the influence of experimental parameters qualitatively and quantitatively. In this model, the incident laser light is considered to be a Gaussian beam that propagates through a three-dimensionally resolved cuvette. A ray tracing approach is implemented to trace the emitted signal rays from the scattering volume through the optical components to the slit of the spectrograph. The model is described in the first part of this paper, and its application to the effects of experimental parameters in enantioselective Raman spectroscopy is presented in the second part. Eventually, a direct comparison between the simplistic 1D and the new model is made to emphasize the differences.

## 2 Numerical model

The detailed model development was done with MATLAB 7.8.0 (R2009a) to ensure compatibility with a variety of older and current versions of the software. The final code is available as supplementary material and free to use provided that the present work is referenced appropriately. The underlying physics and mathematical framework of the model is presented in the following. An overview of the laser propagation and scattering geometry is illustrated in Fig. 1. A laser beam is focused into a cuvette holding the sample. The scattered Raman signal is observed at  $90^\circ$  and traced through a collimating lens, the half-wave plate, a polarizing beam splitter, and focusing lenses, which eventually focus the signal on the slits of spectrographs.

Compared to the previous theoretical work on the esR method [18, 20], the new model is much more advanced. Previously, the laser beam and the signal were treated as one-dimensional lines. In the following, the real situation having a Gaussian beam and a signal collection with a finite solid angle is taken into account in a 3D mathematical framework.

**Fig. 1** Sketch of the modeled Raman measurement geometry for the enantiomeric discrimination. **a** Schematic overview of setup: *L* lens,  $\lambda/2$  half-wave plate, *PBS* polarizing beam splitter. **b** Coordinate system with respect to cuvette holding the sample. **c** Propagation of Gaussian beam through a convex lens with the beam waists and distances indicated. **d** Meshing of the probe volume along the laser beam propagation in polar coordinates



### 2.1 Probe volume and scattering

The laser beam is considered to be a Gaussian beam. Its propagation through a lens is illustrated in Fig. 1c. The intensity profile of the Gaussian beam is given by the following [21]:

$$I(z, r) = I_{\max} * \left( \frac{w_0}{w(z)} \right)^2 * e^{-2 * \frac{r^2}{w(z)^2}}, \tag{1}$$

where  $w(z)$  denotes the local beam width,

$$w(z) = w_0 * \sqrt{1 + \left( \frac{\lambda * z}{\pi * w_0^2} \right)^2}. \tag{2}$$

Furthermore,  $I_{\max}$  is the peak intensity at  $z = 0$  and is calculated from the total power of the applied laser  $P_{\text{laser}}$ , according to

$$I_{\max} = \frac{2 * P_{\text{laser}}}{\pi * w(0)^2}. \tag{3}$$

The intensity profile in front of the focusing lens is set according to Eq. (1) with a known beam waist. A much smaller beam waist and thus a higher local intensity is arising from the focusing of the beam before entering the measuring volume as illustrated in Fig. 1c.

The position  $b$  of the focused beam waist and its magnitude  $w'_0$  are calculated by the lens equation and the complex beam parameters,  $q_1$  and  $q_2$ , according to Eichler and Eichler [21]. With the assumption that the Rayleigh range of the unfocused beam  $z_R \gg (a - f)$ , which is true for the modeled case, the focused beam waist can be calculated by:

$$w'_0 = \frac{\lambda * f}{\pi * w_0}. \tag{4}$$

The position  $b$  of the focused beam waist lies at the entry of the measuring volume, i.e.  $z = 0$  as shown in Fig. 1b. We note that in an experiment, it would be the intention to place the minimal waist in the center of the cuvette. This would mean that the laser beam can be considered as a cylinder in the ideal case. However, deviations from this cylinder shape are realistic and thus we consider a slightly diverging laser beam. In the case considered, the beam diverges only slightly while passing through the cuvette. We note that this does not lead to a significant influence on the results. Equation (4) shows that a wide unfocused beam waist is desirable to obtain a narrow beam after focusing, but  $w_0$  is limited by the size (diameter) of the focusing lens and the initial beam diameter [21].

Figure 1d illustrates how the measuring volume is formed by the incident laser beam. Each of the volume elements, bordered by  $\Delta z$ ,  $\Delta r$  and  $\Delta \phi$ , is considered as a scattering element. Every volume element is specified by a different incident intensity  $I_p$ , length  $l$ , and solid angle  $\Delta \Omega$ . The total power incident on a volume element is obtained by integrating the incident intensity over the surface of the considered volume element formed by  $\Delta \phi$  and  $\Delta r$ . The length of the scattering volume element is  $\Delta z$ .

From each volume element, Raman photons are emitted and a fraction of them is collected by the lens. The corresponding solid angle is the angle under which a surface is seen by a point. Thus, the solid angle can be understood as a cone between the center of a scattering element and

the lens. Mathematically, it is the ratio of the partial area  $A_S$  of the surface of a sphere and the squared radius of this sphere:

$$\Omega = \frac{A_S}{r_S^2}. \tag{5}$$

The partial area, opened up by the semi-axes of the collecting area, which is the effective surface area of the collimator, becomes elliptic for scattering elements not lying in the center of the probe volume. The surface area of an ellipse is:

$$A_S = A_{\text{ellipse}} = \pi * \frac{a_{\text{ep}}}{2} * \frac{b_{\text{ep}}}{2}. \tag{6}$$

When the central scattering element is considered, the first and second axes,  $a_{\text{ep}}$  and  $b_{\text{ep}}$ , are equal in magnitude, and in this case, Eq. (6) turns into the formula for the surface area of a circle. Although the calculated partial area seen from each volume element is planar and not a fraction of a spherical surface, it serves for the calculation of  $\Delta\Omega$ , according to Eq. (5). This assumption holds as the radius of the sphere that encases the particular partial area is much bigger than the first or second axis of the considered surface area, so that the partial area approximates a planar surface. The radius  $r_S$  of the sphere covering the partial area is the distance from the center of the considered scattering element to the center of the corresponding ellipse. The variation of the solid angle for different scattering elements is very small as the actual extent of the measuring volume is much smaller than the distance to the collimator and its diameter.

With the solid angle and the incident intensity, the calculation of the Raman scattered light intensity, emitted from each volume element, becomes possible using the simplified working equation [22, 23]:

$$I_{\text{RS}} = k_{\text{exp}} * \Delta\Omega * \frac{\partial\sigma}{\partial\Omega} * I_i * N * l_{\text{sample}}, \tag{7}$$

where  $\frac{\partial\sigma}{\partial\Omega}$  is the differential Raman cross section,  $N$  the number concentration of the scattering species, and  $k_{\text{exp}}$  an experimental calibration constant.

### 2.2 Signal ray tracing

The signal photons are emitted from the individual volume elements into any direction, and the lens collects only a fraction of them. Moreover, not all of the photons that hit the lens eventually end up in the spectrometer. Therefore, a ray tracing approach based on geometrical optics is used in the following. General methods of analytic geometry [24] enable the calculation of the intersection point  $(X, Y, Z)$  of a skew ray, in vector form, with a spherical or planar surface. This is called the transfer procedure. Furthermore, the new

direction of a refracted ray, after having reached the spherical or planar surface, is determined according to [24]. This is known as refraction procedure.

The transfer procedure of a skew ray to a spherical surface is divided into the transfer to the non-physical plane tangent on the spherical surface and the determination of the intersection point of the ray with the spherical surface. Initially, the calculation of the coordinates at the tangential plane is carried out [24]:

$$Y_T = Y_{-1} + \Delta Y = Y_{-1} + d_{-1} \frac{L_{-1}}{n_{-1}}, \tag{8}$$

$$Z_T = Z_{-1} + \Delta Z = Z_{-1} + d_{-1} \frac{K_{-1}}{n_{-1}}. \tag{9}$$

The coordinate  $X_T$  is zero for convenience. The optical direction cosine  $L_{-1}$  is the product of the direction cosine with the  $y$ -axis and the refractive index  $n_{-1}$  of the medium, in which the transfer procedure takes place. Furthermore,  $K_{-1}$  is the optical direction cosine with respect to the  $z$ -axis. The length of the distance,  $d_{-1}$ , between the origin of the ray and its intersection point with the tangent plane needs to be calculated. The change in the  $X$ -coordinate, taking  $X_T = 0$  into account, is [24]:

$$\Delta X = t_{-1} - X_{-1}, \tag{10}$$

where  $t_{-1}$  denotes the distance of the tangential plane to the origin of the skew ray along the optical axis ( $x$ -axis). Taking the length of the ray,  $d_{-1}$ , and the direction cosine with the  $x$ -axis into account, gives rise to an additional formulation of the change in  $X$ , where  $M_{-1}$  is the optical direction cosine with the  $x$ -axis [24]:

$$\Delta X = d_{-1} \frac{M_{-1}}{n_{-1}}. \tag{11}$$

The combination of Eqs. (10) and (11) enables the calculation of the length of the ray,  $d_{-1}$ , and hence, the coordinates in the tangential plane with Eqs. (8) and (9):

$$d_{-1} = (t_{-1} - X_{-1}) \frac{n_{-1}}{M_{-1}}. \tag{12}$$

The second step is the determination of the intersection point with the spherical surface. The direction cosines of the ray do not change, so the calculation works similar, but this time in terms of the distance  $A$  [24]:

$$X = \frac{A}{n_{-1}} M_{-1}, \tag{13}$$

$$Y = Y_T + \frac{A}{n_{-1}} L_{-1}, \tag{14}$$

$$Z = Z_T + \frac{A}{n_{-1}} K_{-1}, \tag{15}$$

$$\frac{A}{n_{-1}} = \frac{H}{B + n_{-1}\cos(\theta_1)}, \tag{16}$$

where  $\theta_1$  denotes the incident angle of the ray with the surface normal,

$$n_{-1}\cos(\theta_1) = n_{-1}\sqrt{\left(\frac{B}{n_{-1}}\right)^2 - cH}. \tag{17}$$

The parameters  $H$  and  $B$  are calculated according to the following expressions [24]:

$$H = c(Z_T^2 + Y_T^2), \tag{18}$$

$$B = M_{-1} - c(Y_T L_{-1} + Z_T K_{-1}). \tag{19}$$

The curvature  $c$  of the spherical surface is the reciprocal of the radius  $r$ . If the center of curvature lies to the right of the tangential plane, the curvature is defined with a positive sign. In case the center of curvature lies to the left of the tangential plane, the sign becomes negative by definition [24].

To perform the transfer procedure of a skew ray from its origin to a spherical surface, one needs to calculate the values of  $H$ ,  $B$ ,  $n_{-1}\cos(\theta_1)$ , and  $\frac{A}{n_{-1}}$  in exactly this order. Afterwards, the determination of the coordinates of the point of intersection with the spherical surface becomes possible when inserting the previously calculated value of  $A$  to the Eqs. (13–15). When applying the transfer procedure to a planar surface,  $A$  becomes zero and the coordinates of the intersection point are  $X_T$  (which is zero at a tangential plane),  $Y_T$ , and  $Z_T$  [24].

In a next step, the calculation of the altered optical direction cosines  $K$ ,  $L$ , and  $M$  of a skew ray, due to the refraction at a spherical or planar surface, is carried out. The optical direction cosines of the initial ray are denoted as  $K_{-1}$ ,  $L_{-1}$ , and  $M_{-1}$  [24]:

$$M = M_{-1} - (X * c - 1)\Gamma, \tag{20}$$

$$L = L_{-1} - Y * c * \Gamma, \tag{21}$$

$$K = K_{-1} - Z * c * \Gamma, \tag{22}$$

$$\Gamma = -n_1 * \cos(\theta_1) + n_2 \sqrt{\left(\frac{n_1}{n_2} \cos(\theta_1)\right)^2 - \left(\frac{n_1}{n_2}\right)^2} + 1. \tag{23}$$

The optical direction cosines as well as the product of the direction cosines and the particular refractive index of a ray refracted at a planar surface ( $c \rightarrow 0$ ) do not change according to Eqs. (20–22). However, the direction cosines differ as the refractive indices are unequal in front of and behind the refracting surface. In the following, the scattered intensity is apportioned among a certain number of rays, directed towards the collimating lens, according to Fig. 2.

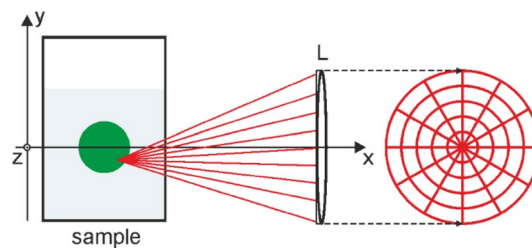


**Fig. 2** Sketch of the irradiated liquid sample emitting Raman scattered light towards the collimating lens. Rays from a certain volume element hit a tangential plane in front of the collimator lens

The resolution of the polar grid in the tangential plane of the collimator, illustrated on the right-hand side of Fig. 2, determines the number of emitted rays from each scattering element. Now, transfer and refraction procedures are carried out to trace the rays through the collimator. The rays are furthermore traced through the half-wave plate. Here, the birefringent property of the half-wave plate needs to be taken into account, according to [25, 26]. At the diagonal plane of the polarizing beam splitter, horizontally and vertically polarized signal is separated from each other. Hence, each ray is separated into a transmitted and a reflected component. For the reflection procedure, the parameter  $\Gamma$  from Eq. (23) becomes [24]:

$$\Gamma = -2 * n_1 * \cos(\theta_1). \tag{24}$$

Finally, each component is traced through a focusing lens towards the spectrometer slit. The rays reaching the spectrometer slit are taken into account in the subsequent intensity calculation.

### 2.3 Polarization-resolved intensity calculation

Now, the fractions of vertically and horizontally polarized scattered light are calculated. First, the angle of rotation due to the optical activity is:

$$\alpha = [\alpha]_{\lambda}^{\theta} * l_{\text{sample}} * c, \tag{25}$$

where  $[\alpha]_{\lambda}^{\theta}$  denotes the specific angle of rotation of the investigated chiral substance to a certain wavelength  $\lambda$  and temperature  $\theta$ , and  $c$  is the concentration. This gives rise to the rotation of the polarization plane of the laser light propagating along the  $z$ -axis. Accordingly, the rotation of the polarization plane of the detected polarized and depolarized signals travelling through the sample along the  $x$ -axis (direction of observation) is carried out. By definition, the (+)-enantiomer rotates the plane of polarization clockwise (watching against the direction of signal propagation). Consequently, the (–)-enantiomer causes an anticlockwise rotation. Thus, the (+)-enantiomer creates a positive angle, the

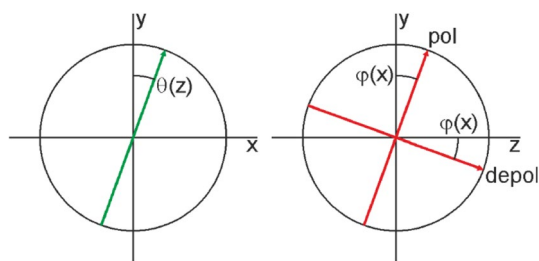


**Fig. 3** Rotation of the polarization plane of the incident laser light when propagating along the z-axis (*left*). Rotation of the polarization plane of the polarized and depolarized Raman signals when propagating along the x-axis (*right*)

(–) enantiomer a negative angle, with the y-axis. Figure 3 illustrates schematically the two rotation events.

On the left-hand side, the rotation of the laser polarization around the z-axis is displayed watching towards the direction of propagation. Likewise, a rotation around the x-axis of the polarized and depolarized components of the scattered light is observed (Fig. 3, right).

Through the three-dimensionally resolved measuring volume and thereby formed scattering volume elements, the path dependence of the rotation angle needs to be taken into account. In general, two parameters determine the ratio of vertically and horizontally polarized signal components in a scattered beam that is eventually detected. First, the concentration and enantiomeric excess of the chiral substance, because they determine the optical activity, and second, the position of the scattering volume element, because it determines how far the laser and the signal have to travel inside the optically active sample. Mixtures of enantiomers of a chiral substance cause a resulting rotation angle through the clockwise and anticlockwise rotation of the two enantiomers:

$$\theta^{(+)(-)} = [\alpha]_{\lambda, \text{norm}}^{\theta} * (c_{\text{norm}, (+)} - c_{\text{norm}, (-)}) * z, \tag{26}$$

$$\varphi^{(+)(-)} = [\alpha]_{\lambda, \text{norm}}^{\varphi} * (c_{\text{norm}, (+)} - c_{\text{norm}, (-)}) * x. \tag{27}$$

In Eqs. (26) and (27), the normalized specific rotation angle (for a normalized concentration of 1) of the (+)-enantiomer is applied. Here,  $c_{\text{norm}}$  denotes the normalized concentration of either the (+)- or (–)-enantiomer of the considered chiral substance and varies between zero and one. A value of one means the maximum concentration of one of the two enantiomers. If both concentrations are one (total, and maximum concentration of two), the solution is considered to be saturated. Moreover, Eqs. (26) and (27) manifest that racemic mixtures lead to a rotation angle of 0°.

The plane of polarization of the scattered Raman signal is further rotated when crossing the half-wave plate, i.e. the symmetry breaking element. According to the definition of the sense of rotation concerning the optical activity of the sample, the sign of the angle created by the optical axis of the half-wave plate and the y-axis is defined. Hence, a clockwise rotation of the optical axis around the x-axis accounts for a positive, an anticlockwise rotation for a negative angle with the y-axis when watching against the direction of propagation. The angle that the polarization plane of the incident scattered light creates with the optical axis is doubled. In this case, the optical axis lies within the y–z plane:

$$\varphi_{\text{new}} = \varphi - 2 * (\varphi^{(+)(-)} - \psi), \tag{28}$$

where  $\varphi_{\text{new}}$  is the angle between the polarization plane of the Raman signal after passing through the half-wave plate and the y-axis. Moreover,  $\psi$  is the angle created by the optical axis of the half-wave plate and the y-axis. Please note that in the previous work [18, 20], there was a small mistake in the corresponding equation leading the systematically altered angles (the observed effects were the same though, just at different absolute angles).

In a next step, the already calculated total scattered intensity  $I_{\text{RS}}$  of a volume element for a given enantiomeric concentration is split into its polarized and depolarized components. With the known depolarization ratio  $\rho$  of the considered vibrational state, the determination of the polarized and depolarized intensity from the total scattered intensity is enabled:

$$I_{\text{RS}} = I_{\text{pol}} + I_{\text{depol}}, \tag{29}$$

$$\rho = \frac{I_{\text{depol}}}{I_{\text{pol}}}. \tag{30}$$

Depolarized light is defined as the fraction of scattered light that is perpendicularly polarized to the polarization plane of the exciting laser [27]. Knowing the magnitude of polarized and depolarized scattered intensities and the corresponding angle with the y-axis of each scattering element for a certain enantiomer concentration makes the calculation of the vertically and horizontally polarized intensity components  $I_v$  and  $I_h$  possible [19], taking into account Malus’s law [28]:

$$I_v(x,z) = I_{\text{pol}} \cos(\theta(z))^2 \cos(\varphi(x))^2 + \frac{I_{\text{depol}}}{2} \sin(\theta(z))^2 \cos(\varphi(x))^2 + \frac{I_{\text{depol}}}{2} \sin(\varphi(x))^2, \tag{31}$$

$$\begin{aligned}
 I_h(x,z) = & I_{\text{pol}} \cos(\theta(z))^2 \sin(\varphi(x))^2 \\
 & + \frac{I_{\text{depol}}}{2} \sin(\theta(z))^2 \sin(\varphi(x))^2 \\
 & + \frac{I_{\text{depol}}}{2} \cos(\varphi(x))^2.
 \end{aligned} \tag{32}$$

In a last step of the model development, the ray tracing procedure and the intensity calculation are combined. As already mentioned, the scattered intensity of a volume element is evenly distributed onto its emitted rays towards the collimator. This is justified for practically relevant numerical apertures. For a certain enantiomeric composition, the scattered horizontally polarized light intensity of the entire measuring volume is carried by the rays transmitted by the beam splitter and propagating towards spectrometer 1. The intensity portions of all rays that reach the spectrometer slit are added together. The remaining rays that do not reach the slit are neglected and their carried intensity value is set to zero as it is not detected. The same is done for the rays that propagate towards spectrometer 2, carrying vertically polarized light. Thereby, the total horizontally and vertically polarized intensities are obtained for a specific enantiomeric composition. The calculation for several compositions yields the intensity distribution over the normalized concentrations of the two enantiomers. This enables the qualitative analysis of enantiomeric discrimination.

### 3 Results and discussion

The model has been used to study how different experimental parameters influence the horizontally and vertically polarized signal intensities. A key point is to check how the consideration of a 3D geometry compares to the previous 1D results [18, 20]. This is also important for evaluating the potential limitations when the esR technique is applied in an experiment. Normalized Raman intensities are calculated in dependence on the normalized enantiomer concentrations with systematic variation of the most influential parameters. The considered parameters are the orientation of the optical axis of the half-wave plate, the specific angle of rotation/sample length, the depolarization ratio, and obviously the concentration of the investigated species. In the following, the labeled intensity is a normalized value, which is the ratio of the intensity scattered by a certain enantiomer composition and a reference intensity, defined in the particular section. Thereby, parameters that exclusively influence the absolute scattered intensity might be neglected in this analysis, focusing on the possibility of discriminating between two enantiomers. Moreover,

normalized concentrations are applied, where the maximum concentration ( $c_{(+)}=1$ ,  $c_{(-)}=1$ ) represents a solution saturated with the chiral substance. If not declared differently, the expression rotation angle in the following sections denotes exclusively the angle  $\varphi$ , which accounts for a rotation of the polarization plane of the scattered signal around the  $x$ -axis and is modified by the half-wave plate. With the applied parameters, a maximum concentration of either the (+)- ( $c_{(+)}=1$ ,  $c_{(-)}=0$ ) or (–)-enantiomer ( $c_{(+)}=0$ ,  $c_{(-)}=1$ ) yields an angle of rotation of the signal of  $+10^\circ$  or  $-10^\circ$ , respectively.

#### 3.1 Half-wave plate orientation

Due to the default settings of the model parameters, the beam waist of the focused Gaussian beam is in the range of about  $10^{-5}$  m, so that all the signals emitted by scattering elements of the measuring volume pass approximately through the half-width of the cuvette. Thus, their polarization planes are rotated about the same extent. The depolarization ratio is chosen as 0.1 by default and the sample length/width is 10 mm, which is the dimension of a typical cuvette. It should be taken into account that the set depolarization ratio is an arbitrary value. The depolarization ratio can basically vary between 0 and 0.75 for non-depolarized and fully depolarized modes [29]. The influence of an increasing depolarization ratio, for different species and Raman modes, is presented in Sect. 3.3. According to the geometry parameters, introduced in Fig. 1, the length of the measuring volume is divided into 15 parts. The radius and angle of each length segment are divided into ten parts. Angle and radius of the polar grid of the collimator are divided into eight parts, according to Fig. 2. Figure 4 illustrates the distributions of horizontally and vertically polarized intensities as function of the enantiomer composition for half-wave retarder orientations from  $0^\circ$  to  $-10^\circ$ . The illustrated normalized intensities to a certain half-wave retarder orientation are obtained by dividing the calculated absolute value by the maximum value of the particular vertically polarized intensity. In case the optical axis coincides with the  $y$ -axis, as shown in the top panels of Fig. 4, it is not possible to discriminate the two enantiomers unambiguously. Here, two different enantiomeric compositions, i.e.,  $c_{(+)}=0.75$ ,  $c_{(-)}=0.25$ , and  $c_{(+)}=0.25$ ,  $c_{(-)}=0.75$ , result in two pairs of horizontally and vertically polarized intensity of the same magnitude. For the two samples, the polarization planes of the signals are rotated into opposite directions, but by the same magnitude, so that the fractions of the polarization components are equal. The symmetry plane, causing this equivalence, is parallel to the  $y$ -axis and contains the equimolar line ( $c_{(+)}=c_{(-)}$ ). The equimolar line represents racemic mixtures that exhibit a resulting angle of rotation of  $0^\circ$  with the  $y$ -axis.

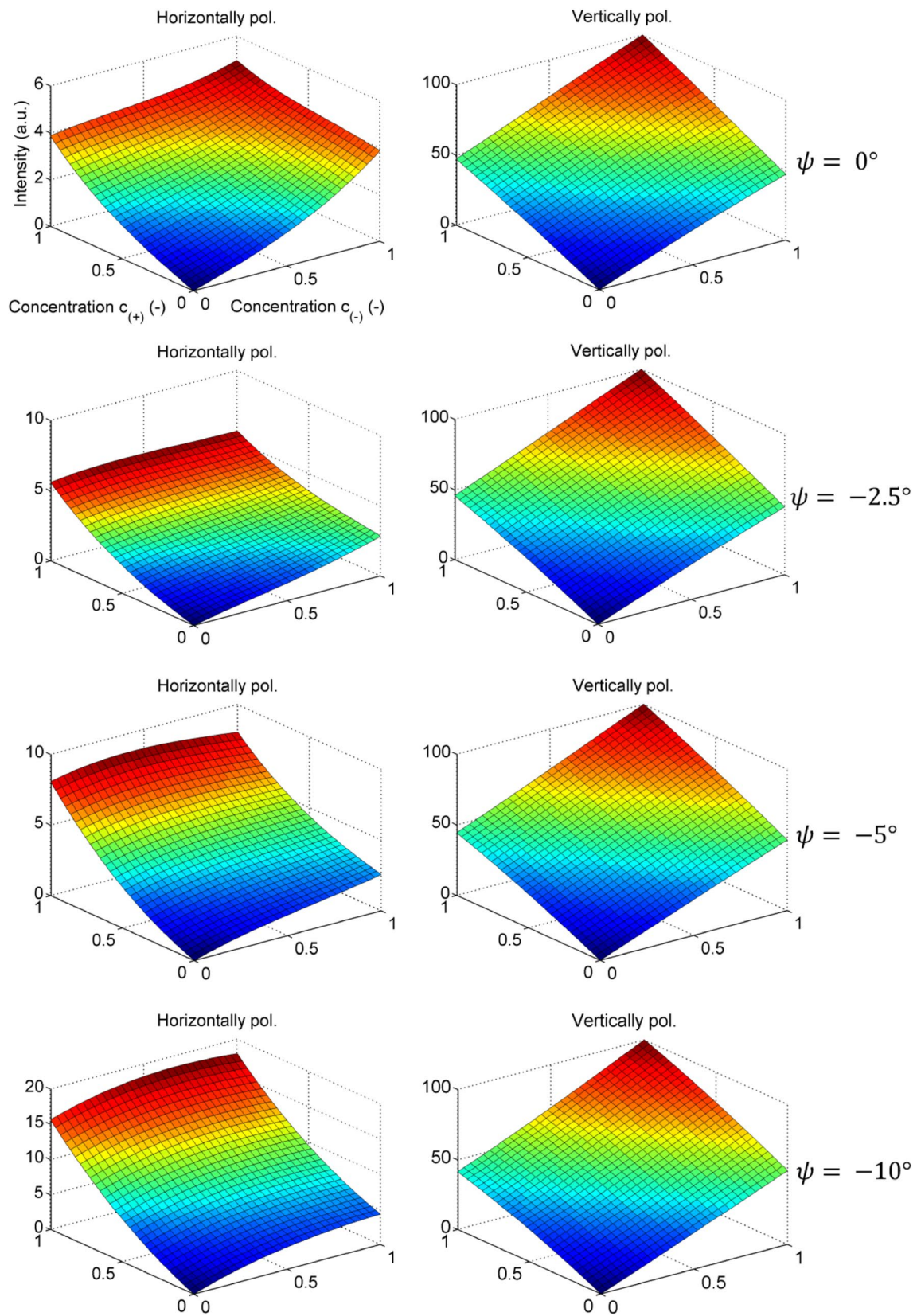


**Fig. 4** Vertically and horizontally polarized normalized intensities plotted against normalized enantiomer concentrations for an increasing angle created by the optical axis of the half-wave plate and the y-axis (top to bottom)



In this case, the polarized component coincides with the  $y$ -axis and has no horizontally polarized component, which is exclusively governed by the comparatively weak depolarized signal (depolarization ratio of 0.1). Non-racemic compositions yield a resulting angle of rotation unequal to zero and, therefore, a component of the strong polarized component in the horizontally polarized intensity. However, determination of the overall concentration of the investigated chiral species is possible by comparing the sum of the two intensities for a certain composition to a corresponding calibration curve of the investigated species. When the retardation plate is rotated in a way that the angle created with the  $y$ -axis is  $-2.5^\circ$ , the symmetry line is shifted towards compositions that exhibit an excess of the  $(-)$ -enantiomer, see Fig. 4. The symmetry line contains samples that lead to an overlap of the polarized and depolarized signal with the coordinate axes.

Figure 5 illustrates the rotation procedure for two different samples lying on opposing sides of the symmetry line. The resulting orientations of the polarized and depolarized signals exhibit the same absolute components in the detected intensities. Hence, it is not possible to differentiate between the two samples for this half-wave retarder orientation. Surprisingly, the horizontally polarized intensity to the  $\psi = -5^\circ$  does not exhibit a symmetry line anymore. There is only one mixture configuration that causes the coincidence of the polarized and depolarized signals with the coordinate axes in this case, which is a sample

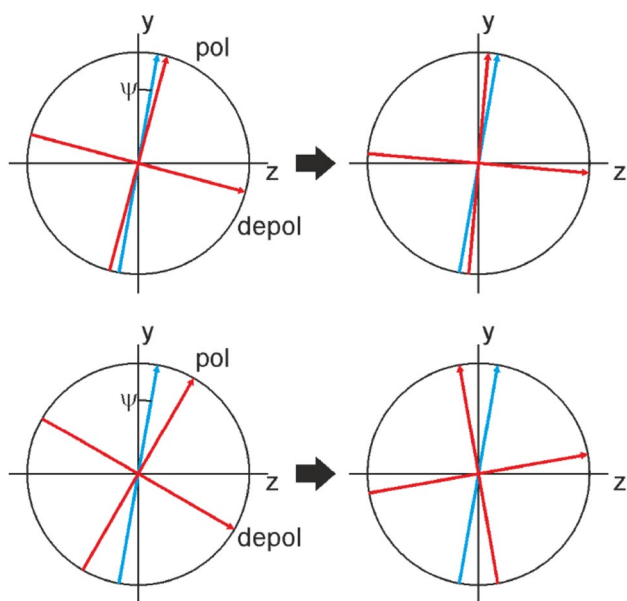


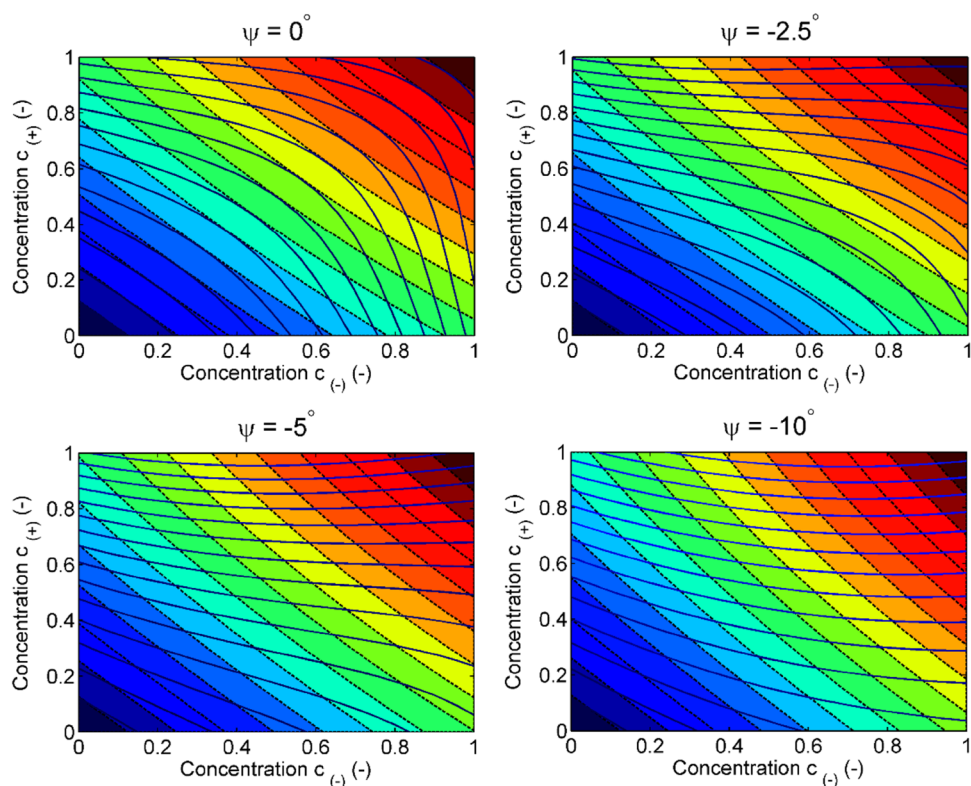
**Fig. 5** Polarization plane orientation of polarized and depolarized signals for a half-wave retarder orientation of  $\psi$  and two different samples (*top* and *bottom*). Resulting signal orientations exhibit the same magnitude of the absolute *horizontally* and *vertically* polarized components

containing exclusively the  $(-)$ -enantiomer at the maximum concentration. This yields, according to the defined parameters in the beginning of this section, an angle of rotation of  $-10^\circ$ . According to Eq. (28), this results in an angle of  $0^\circ$  with the  $y$ -axis after passing through the half-wave plate. In this case, the lack of a symmetry element within the distribution of the horizontally polarized intensity enables the unambiguous assignment of samples to a certain pair of horizontally and vertically polarized intensity.

A half-wave retarder orientation of  $\psi = -10^\circ$ , presented in the bottom panels of Fig. 4, yields an even higher gradient within the horizontally polarized intensity and might further improve the discrimination for different samples. An optimal half-wave retarder orientation depends on the absolute magnitude of Raman scattered signal in a particular experiment and on how easily two intensity pairs of different enantiomer samples might be distinguished. This, in turn, depends on the sensitivity of the applied camera sensor. Another limitation is the coincidence of the vertically polarized signal component with the  $z$ -axis, which would lead to an undesired symmetry. The higher gradient of the horizontally polarized intensity arises from an increasing influence of the polarized signal. In general, the vertically polarized intensity changes only slightly with increasing orientation angle of the half-wave plate. This is due to the fact that the strong cosine component of the polarized signal [see Eqs. (30, 31)] is the major part of the vertically polarized intensity. Hence, the comparatively small rotations of the polarized signal within an interval from  $-30^\circ$  to  $10^\circ$  for different enantiomeric compositions after having passed through the half-wave retarder lead to similar intensity profiles on the right-hand side of Fig. 4.

The iso-intensity contour lines to the four half-wave retarder orientations in Fig. 6 affirm the aforementioned insight. A solid line connects all enantiomeric concentration pairs,  $c_{(+)}$  and  $c_{(-)}$ , that yield a certain intensity of the horizontally polarized signal. Respectively, the dashed lines connect enantiomeric compositions that lead to a certain intensity of vertically polarized signal. The figure confirms the finding about enantiomeric discrimination in dependence on the orientation of the optical axis. The panels for  $\psi = 0^\circ$  and  $-2.5^\circ$  illustrate that a solid line might have two intersection points with a dashed line. In this case, there exist two enantiomeric concentration pairs that lead to the same magnitude in horizontally and vertically polarized intensities. Enantiomeric discrimination is impossible in this case. Due to the lack of a symmetry plane in the horizontally polarized intensity, an orientation angle of  $\psi = -5^\circ$  or  $-10^\circ$  enables enantiomeric discrimination without any doubt as each enantiomeric composition corresponds to a unique pair of intensities. This case is shown in the bottom panels of Fig. 6, where each solid line exhibits exactly one intersection point with each dashed line.

**Fig. 6** Contour lines of iso-intensity of vertically (dashed lines) and horizontally (solid lines) polarized signal components to four different investigated half-wave plate orientations

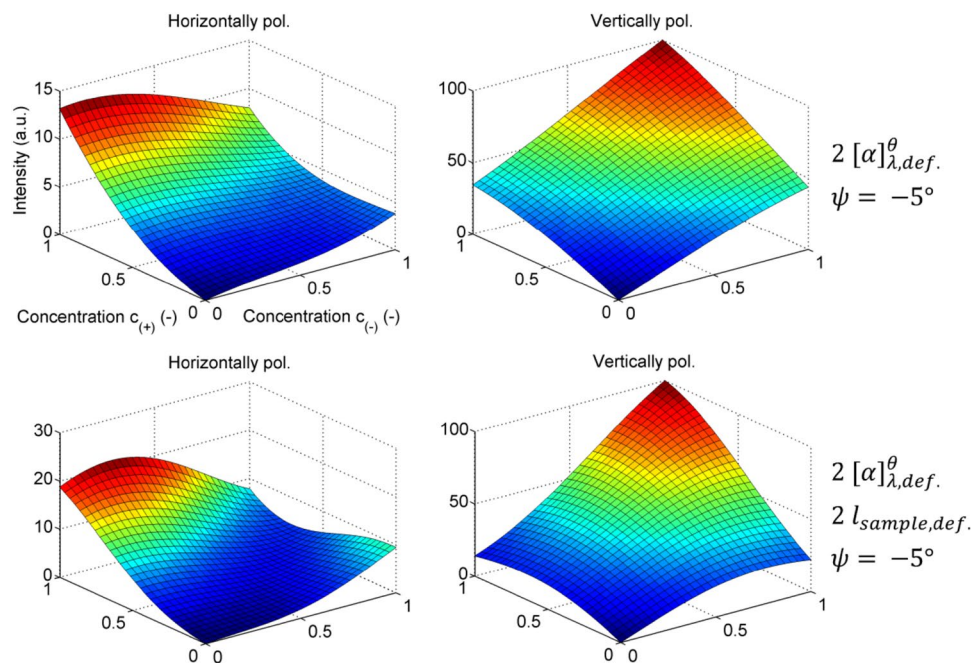


Furthermore, the sum of the two polarization components gives rise to the overall concentration of the investigated substance. Note that the variation of the retarder orientation angle from 0° to 10° leads to similar results when exchanging (+)- and (-)-enantiomer in the previous discussion.

### 3.2 Specific angle of rotation and sample length

The investigation of the influence of the specific angle of rotation and the sample length on the enantiomeric discrimination is carried out in this section. Taking Eq. (25) into account clarifies that both the specific angle of rotation

**Fig. 7** Vertically and horizontally polarized normalized intensities plotted against normalized enantiomer concentrations for twofold specific angle of rotation (top), and twofold specific angle of rotation plus twofold sample length (bottom). The half-wave retarder orientation is kept constant



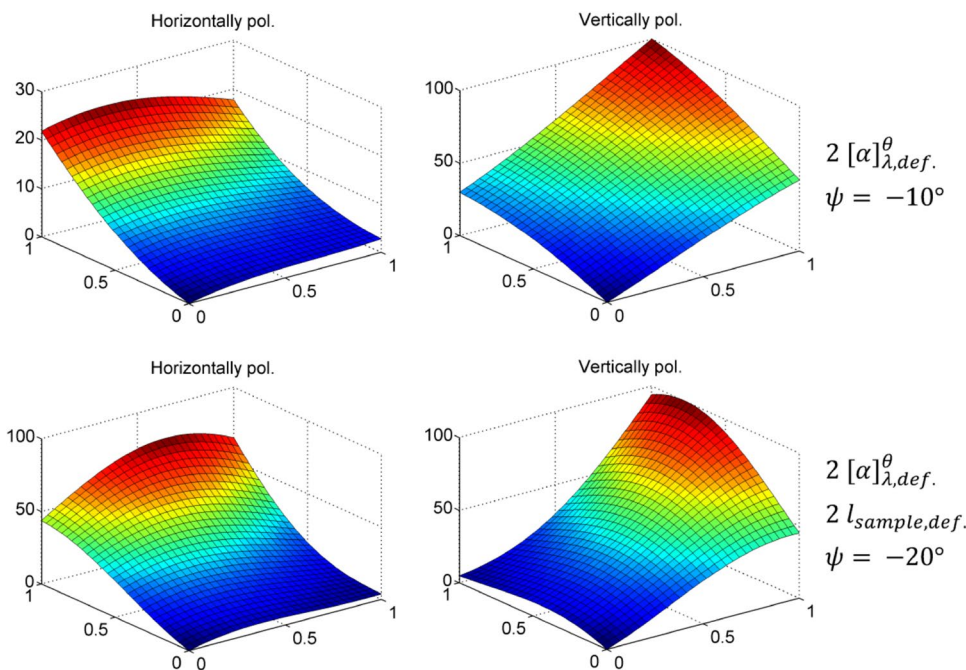
and the sample length are proportional to the resulting angle of rotation. Thus, a double specific angle of rotation, i.e., for a different investigated species, or a double sample length (2 cm) results in an angle of rotation twice in magnitude. Furthermore, a variation of the specific angle of rotation or the sample length requires different orientation angles  $\psi$  to avoid the occurrence of a symmetry plane within the distribution of horizontally polarized intensity. The top panels of Fig. 7 (first case) show the results for a specific angle of rotation twice as high as the default value. The bottom panels illustrate the results of the second case, calculated with the twofold specific angle of rotation and a twofold sample length. Hence, the angles of rotation of a signal originating from the center of the cuvette in a solution with either the maximum concentration of the (+)- or (-)-enantiomer become  $20^\circ/-20^\circ$  for the first case and  $40^\circ/-40^\circ$  for the second case, respectively. According to the previous section, the maximum value of the vertically polarized intensity is chosen as the reference value in the intensity normalization in both cases. Due to the generally higher resulting rotation angles, compared to the previous section, the surfaces in Fig. 7 exhibit a higher nonlinearity. Therefore, the horizontally polarized intensity is more dependent on the orientation of the polarized component. Applying a half-wave retarder orientation angle of  $\psi = -5^\circ$  does not generate a coincidence of the polarized signal component with the y-axis for a maximum concentration of the (-)-enantiomer. According to the previous section, enantiomer pairs that yield an angle of rotation of  $-10^\circ$  lead to the overlap with the coordinate axis and thus lead to the symmetry plane in the horizontally polarized intensity

as shown on the left-hand side of Fig. 7. A larger resulting angle of rotation as applied in the second case leads to a shift of the minimum line towards compositions with an even lower excess of the (-)-enantiomer for  $\psi = -5^\circ$ .

In both cases, the normalized vertically polarized intensity decreases for enantiopure samples of maximum concentration with rising resulting angles of rotation. These samples lead to the highest resulting rotation angles. Hence, the influence of their polarized component on the vertically polarized intensity decreases with increasing rotation angles. Unambiguous enantiomeric discrimination becomes possible when the symmetry in the distribution of the horizontally polarized intensity disappears. This effect occurs, according to the previous section, when the orientation angle of the half-wave retarder is half as high as the angle of rotation generated by an enantiopure sample with maximum concentration. Then, the polarized signal component overlaps with the y-axis after having crossed the half-wave plate. In case one, the sample  $c_{(+)}=0, c_{(-)}=1$  generates an angle of rotation of about  $\varphi = -20^\circ$  with the y-axis, so that the half-wave plate is rotated to  $\psi = -10^\circ$ . Correspondingly, it is rotated to  $\psi = -20^\circ$  to provoke the same effect in case two for the same sample ( $\varphi = -40^\circ$ ). Figure 8 illustrates the resulting distributions of horizontally and vertically polarized intensity components for the two aforementioned cases.

Apparently, both cases provide a doubtless enantiomeric discrimination with the appropriate half-wave plate orientation. The crucial difference to the cases shown in the previous section is that the vertically polarized signal component reaches much smaller values, especially for the sample

**Fig. 8** Vertically and horizontally polarized normalized intensities plotted against normalized enantiomer concentrations for twofold specific angle of rotation (top) and twofold specific angle of rotation and sample length (bottom). The half-wave retarder orientation is varied



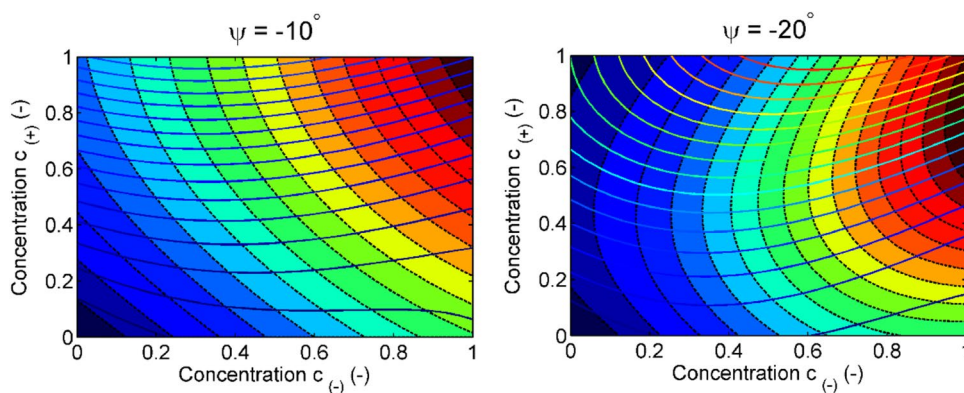
$c_{(+)} = 1, c_{(-)} = 0$ . For this sample, the polarized signal component creates the lowest possible angle with the  $z$ -axis, which accounts for the horizontally polarized intensity. The maxima in the horizontally and vertically polarized intensities for the second case arise from the increasing influence of the resulting rotation angle, as the intensities become more governed by the particular orientation of the strong polarized signal. Hence, the comparatively strong rotations, arising from rotation angles between  $-80^\circ$  and  $0^\circ$  after having passed through the half-wave retarder, lead to a shift of the maximum within the vertically polarized intensity away from the sample  $c_{(+)} = 1, c_{(-)} = 1$ . It is shifted to samples that exhibit a slightly reduced fraction of the (+)-enantiomer.

Figure 9 illustrates the corresponding iso-intensity contour lines. Both diagrams demonstrate schematically the

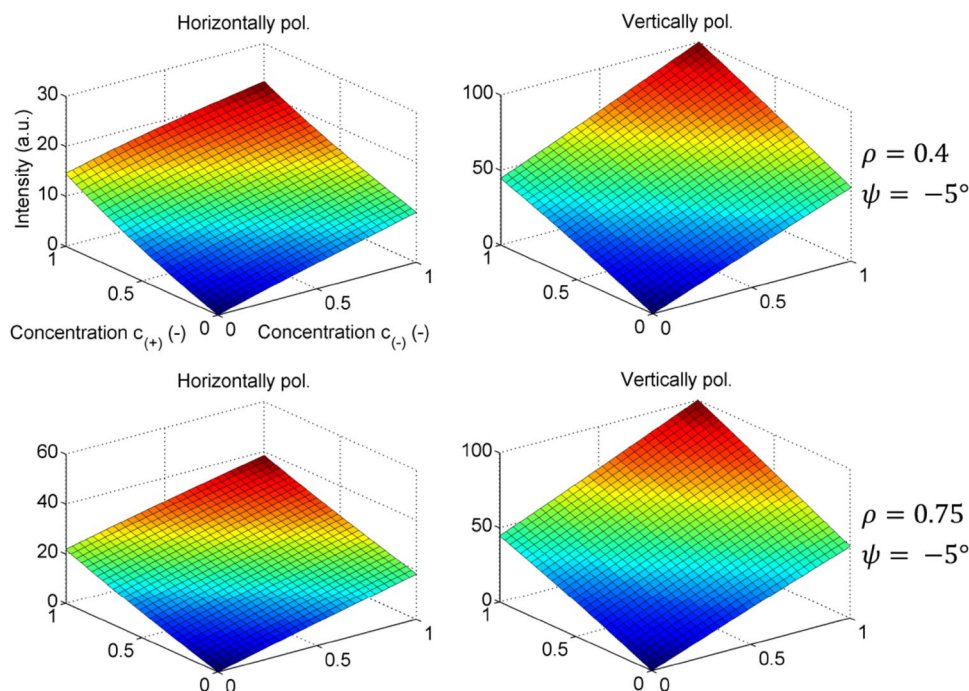
doubtless determination of the enantiomeric composition because of the unique intersection points between the contour lines of the obtained horizontally and vertically polarized intensity. An even larger angle of rotation (i.e.  $3[\alpha]_{\lambda, \text{def.}}^\theta$ ) might prevent unambiguous enantiomeric discrimination, even for an appropriate half-wave retarder orientation. In this case, the polarized signal would coincide with the  $z$ -axis for certain enantiomer compositions and hence lead to a minimum within the vertically polarized intensity. However, it should be taken into account that the assumed theoretical value for the specific angle of rotation, twice as high as the default value, of about  $222.8 \frac{\text{cm}^3}{\text{cm g}}$

for the two investigated cases is an uncommon value. Moreover, the sample length of a conventional cuvette is 1 cm.

**Fig. 9** Contour lines of iso-intensity of vertically (dashed lines) and horizontally (solid lines) polarized signal components to two different angles of rotation and half-wave retarder orientations



**Fig. 10** Vertically and horizontally polarized normalized intensities plotted against normalized enantiomer concentrations for two different depolarization ratios



### 3.3 Depolarization ratio

The depolarization ratio is another parameter evidently influencing the distribution of horizontally and vertically polarized intensity, according to Eqs. (31, 32). The model parameters, except for the depolarization ratio, are set according to Sect. 3.1 with a retarder orientation of  $\psi = -5^\circ$ . Fig. 10 shows the results generated for the arbitrarily chosen depolarization ratios of 0.4 and 0.75. It should be noticed that the depolarization ratio cannot exceed a value of 0.75.

An increasing depolarization ratio means that the polarized component becomes less governing in the intensity calculation. When applying a depolarization ratio of 0.75, almost 43% of the total scattered signal is depolarized. For a depolarization ratio of 0.4, about 29% of the total signal is depolarized. Comparing the results in Fig. 10 to the bottom panels of Fig. 4, simulated with a depolarization ratio of 0.1, leads to the insight that an increasing depolarization ratio causes a higher relative horizontally polarized intensity in the given case. Considering the sample  $c_{(+)}=0$ ,  $c_{(-)}=1$  in the two cases shown in Fig. 10, illustrates the increasing horizontal signal component due to an increasing depolarization ratio. When analyzing samples with an excess of the (+)-enantiomer, the signal components do not overlap with the coordinate axes for the applied half-wave plate orientation. In this case, the depolarized signal creates an angle  $\varphi_{\text{new}}$  between  $-10^\circ$  and  $-20^\circ$  for different compositions with the  $z$ -axis after having passed through the half-wave plate. Thus, an increasing depolarization ratio gives rise to an increasing horizontally polarized intensity as well. The maximum ratio of 0.75 yields similar fractions of the polarized and depolarized components, 57 and 43%, respectively. Hence, the horizontally polarized intensity is less dependent on the orientation of one of the two signal components, so that the rotation angle  $\varphi$  becomes less governing in the gradient of the horizontally polarized intensity profile. Mainly, the total concentration of the investigated substance determines the magnitude of the horizontally

polarized intensity for high depolarization ratios, as shown in Fig. 10.

Figure 11 illustrates the contour lines of the vertically (dashed) and horizontally (solid) polarized intensities for the two investigated depolarization ratios. Although the intensity profile of the horizontally polarized signal becomes more linear and symmetric, the enantiomer composition can be determined unambiguously for a certain pair of intensities. When the sample exhibits a depolarization ratio of 0.75, a further rotation of the optical axis of the half-wave plate might facilitate enantiomeric discrimination even more.

### 3.4 Comparison of simplistic 1D and new 3D model

To emphasize how the new model differs from the previous 1D approach, a few results have been compared directly. There are two main mathematical differences. The predominant difference is the consideration of one vs. three dimensions. The second difference is the implementation of Malus's law in the description of the beam splitter. In the simplistic 1D model, the split of the two polarization components was considered as the absolute values of sine and cosine. This is sufficient for demonstrating the effects qualitatively, but a direct comparison with experimental data is not useful, because the polarized and depolarized intensity components can add up to values beyond the incident intensity.

For the comparison, the one-dimensional case was simulated by reducing the beam radius to  $10^{-9}$  m. Furthermore, the dimensions of all optical components, except for the cuvette, are reduced to  $2 \cdot 10^{-9}$  m. In this case, the scattering occurs exclusively in one point located in the center of the cuvette. To simulate a three-dimensional geometry, the beam waist, which opens up the measuring volume, is increased to 0.01 m. The edge length of the cuvette is increased to 0.02 m for this study. The wider beam is necessary to simulate a three-dimensional geometry, as in the previous sections, a focused beam with a beam waist in the range of  $10^{-5}$  m was applied. For the comparison,

**Fig. 11** Contour lines of iso-intensity of vertically (dashed lines) and horizontally (solid lines) polarized signal components for two different depolarization ratios

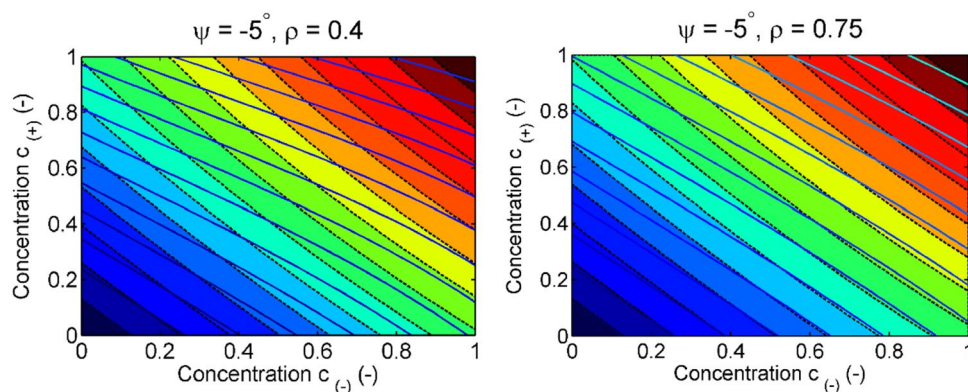
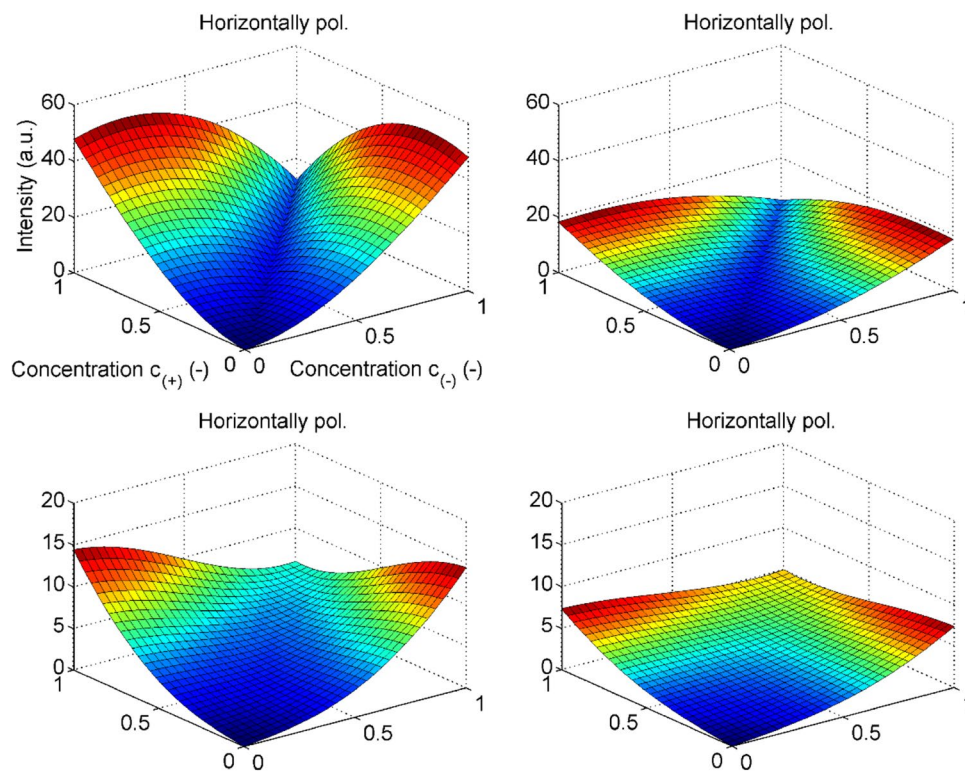


**Fig. 12** Comparison of the 1D and 3D models taking the *horizontal* signal component and a half-wave plate orientation of  $\psi = 0^\circ$  as an example. *Left and right column* represent 3D and 1D respectively. *Upper and lower rows* represent the cases without and with implementation of Malus's law, respectively



the half-wave plate orientation is set to  $\psi = 0^\circ$ . Moreover, both geometries are tested with and without Malus's law implemented. This leads to four different cases: (1) 1D without Malus's law, (2) 3D without Malus's law, (3) 1D with Malus's law, and (4) 3D with Malus's law.

Figure 12 illustrates the direct comparison of the four possible cases for the horizontally polarized signal component. The upper diagrams show the 1D (right) and 3D (left) model without Malus's law. The absolute sine and cosine values result in a sharp edge for  $c_{(+)} = c_{(-)}$ . Qualitatively, both diagrams look identical, but the intensities are higher for the 3D case. The lower diagrams show the 1D (right) and 3D (left) model with Malus's law. There is still a distinct separation at  $c_{(+)} = c_{(-)}$ , but the transition is smooth which is more realistic. Again, qualitatively, both diagrams look identical, but also here, we observe higher intensities for the 3D case.

This comparison shows that the new model represents a substantial advancement over the previous 1D model. It also shows that the previous model is not suitable for a direct comparison of the results with experimental data.

## 4 Conclusion

A ray tracing-based model for the simulation of light scattering experiments was presented in this work and it was used to investigate the effects of experimental parameters in

enantioselective Raman (esR) spectroscopy. In the model, the laser beam is considered in 3D as a Gaussian beam. The light scattered from the different volume elements illuminated by the laser is traced through the optical components of the signal collection system. The results indicate that the enantioselective characteristics of the method that were proposed for 1D are still valid in a 3D geometry. The difference in magnitude between the normalized horizontally and vertically polarized signal components is reduced compared to the idealized case. This is very promising for the practical application of the esR technique. The investigation carried out in this work points out that it can be applied for a broad range of settings and substances. In general, the angle between the optical axis of the half-wave plate and the  $y$ -axis,  $\psi$ , should fulfill the requirement  $\psi = \pm 0.5\varphi$ , so that unambiguous discrimination becomes possible.

Further improvement of the model is generally possible, e.g., by implementing Fresnel equations rather than assuming thin lenses and plain geometrical optics. The implementation of aberration effects would mean an advancement as well. The consideration of wavelength dependencies would be another extension. However, the present model is absolutely sufficient to perform systematic studies of the effects of optical components and their orientation in the setup.

**Acknowledgements** The model implemented as Matlab code is available online as supplementary material. It is free to use and we would like to ask the users that they reference the present work when

publishing results obtained with the code. The authors gratefully acknowledge funding of this work by Deutsche Forschungsgemeinschaft (DFG) through Grant KI1396/4-1.

## References

1. S. Declerck, Y.V. Heyden, D. Mangelings, J. Pharm. Biomed. Anal. **130**, 81–99 (2016)
2. J.R. Cossy, The importance of chirality in drugs and agrochemicals. in *Comprehensive Chirality* (Elsevier, Amsterdam, 2012), pp. 1–7
3. E. Francotte, W. Lindner, R. Mannhold, H. Kubinyi, G. Folkers, Chirality in drug research. in *Methods and principles in medicinal chemistry* (Wiley, Hoboken, 2007)
4. H. Noguchi, M. Takafuji, V. Maurizot, I. Huc, H. Ihara, J. Chromatogr. A **1437**, 88–94 (2016)
5. T. Eriksson, S. Bjorkman, B. Roth, P. Hoglund, J. Pharm. Pharmacol. **52**, 807–817 (2000)
6. C.P. Miller, J.W. Ullrich, Chirality **20**, 762–770 (2008)
7. H.-J. Federsel, Chirality **15**, 128–142 (2003)
8. Y. Qi, D. Liu, W. Zhao, C. Liu, Z. Zhou, P. Wang, Pestic. Biochem. Physiol. **125**, 38–44 (2015)
9. D. Nasipuri, *Stereochemistry of organic compounds: principles and applications* (Wiley, Hoboken, 1994)
10. D. Parker, Chem. Rev. **91**, 1441–1457 (1991)
11. P.J. Stephens, F.J. Devlin, J.J. Pan, Chirality **20**, 643–663 (2008)
12. L.A. Nafie, B.E. Brinson, X.L. Cao, D.A. Rice, O.M. Rahim, R.K. Dukor, N.J. Halas, Appl. Spectrosc. **61**, 1103–1106 (2007)
13. L.D. Barron, L. Hecht, E.W. Blanch, A.F. Bell, Prog. Biophys. Mol. Biol. **73**, 1–49 (2000)
14. L.D. Barron, A.D. Buckingham, Chem. Phys. Lett. **492**, 199–213 (2010)
15. D. Sofikitis, L. Bougas, G.E. Katsoprinakis, A.K. Spiliotis, B. Loppinet, T.P. Rakitzis, Nature **514**, 76–79 (2014)
16. Y. Wang, Z. Yu, W. Ji, Y. Tanaka, H. Sui, B. Zhao, Y. Ozaki, Angew. Chem. Int. Ed **53**, 13866–13870 (2014)
17. D. Patterson, M. Schnell, J.M. Doyle, Nature **497**, 475 (2013)
18. J. Kiefer, K. Noack, Analyst **140**, 1787–1790 (2015)
19. J. Kiefer, M. Kaspereit, Anal. Methods **5**, 797–800 (2013)
20. J. Kiefer, Analyst **140**, 5012–5018 (2015)
21. J. Eichler, H.J. Eichler, *Laser*, 4th edn. (Springer, Berlin, 2002)
22. J. Kiefer, Energies **8**, 3165–3197 (2015)
23. C. Eckbreth, *Laser diagnostics for combustion temperature and species*, 2nd edn. (Gordon and Breach, Amsterdam, 1996)
24. R.E. Hopkins, Fundamental methods of ray tracing. in *Military standardization handbook: optical design* (US Defence Supply Agency, Washington, 1962)
25. M. Avendaño-Alejo, O.N. Stavroudis, A.R.B. Goitia, J. Opt. Soc. Am. A **19**, 1668–1673 (2002)
26. M. Avendaño-Alejo, O.N. Stavroudis, J. Opt. Soc. Am. A **19**, 1674–1679 (2002)
27. D. Brendel, D.A. Skoog, S. Hoffstetter-Kuhn, J.J. Leary, *Instrumentelle Analytik: Grundlagen – Geräte - Anwendungen*. (Springer, Berlin Heidelberg, 2013)
28. P. Williamson, J. Kiefer, Opt. Commun. **372**, 98–105 (2016)
29. D.J. Gardiner, H.J. Bowley, P.R. Graves, D.L. Gerrard, J.D. Loudon, G. Turrell, *Practical Raman spectroscopy* (Springer, Berlin, 2012)